Three-dimensional imaging lidar system based on high speed pseudorandom modulation and photon counting

Yufei Zhang (张宇飞)[1,2], Yan He (贺 岩)[1,*], Fang Yang (杨 芳)[3], Yuan Luo (罗 远)[1,2], and Weibiao Chen (陈卫标)[1,]**

[1]*Key Laboratory of Space Laser Communication and Detection Technology, Shanghai Institute of Optics and Fine Mechanics, Chinese Academy of Sciences, Shanghai 201800, China*

[2]*University of Chinese Academy of Sciences, Beijing 100049, China*

[3]*School of Electronics and Information Engineer, Shanghai University of Electric Power, Shanghai 200090, China*

**Corresponding author: heyan@siom.ac.cn; **corresponding author: wbchen@mail.shcnc.ac.cn*

Received March 31, 2016; accepted September 9, 2016; posted online November 5, 2016

High speed pseudorandom modulation and photon counting techniques are applied to a three-dimensional imaging lidar system. The specific structure and working principle of the lidar system is described. The actual detector efficiency of a single-photon detector in an imaging system is discussed, and the result shows that a variety of reasons lead to the decrease in detection efficiency. A series of ranging and imaging experiments are conducted, and a series of high-resolution three-dimensional images and a distance value of 1200 m of noncooperative targets are acquired.

OCIS codes: 110.6880, 280.3400, 030.5260.
doi: 10.3788/COL201614.111101.

There is an increasing need for three-dimensional imaging systems to acquire range and surface profile data for a number of industrial and defense applications[1]. In recent years, a lot of three-dimensional imaging systems based on different technology have been proposed[2,3]. Among the many methods, pseudorandom (PN) code lidar is a low-power approach to active range resolution and three-dimensional imaging. Traditional three-dimensional imaging systems are mostly composed of low-frequency, high-energy short-pulse-width lasers, large receiver telescopes, and linear detectors[4,5]. However, such a system requires high peak power of the laser to achieve long range imaging[6,7]. Compared to mono-pulse lidar transmitters, the demand for peak power is reduced when a continuous wave laser is modulated by a PN code. So, it can effectively reduce the power consumption, volume, and requirements of the heat dissipation. Because of this advantage, many simulations and experimental investigations on PN code lidar were conducted in ranging or imaging systems[8–12].

PN codes have great potential in applications because of their randomness, sharp autocorrelation, and small cross-correlation value. The PN receiver can measure the signal propagation time and target impulse response by correlating the received signal with the transmitted ones and determining the peak location of the correlation function[13].

A single-photon detector is sensitive enough to detect the weakest light, which allows the lidar system to be operated in an eye-safe level. In recent years, a lot of work on photon counting laser ranging has been done[14–17]. From these works, we can see that these systems need a long pixel dwell time to achieve a histogram. The pixel dwell time of a PN code lidar only depends on the range ambiguity and pulse repetition frequency. Thus, photon counting technology in conjunction with PN codes allows for the lower peak power laser illumination and shorter pixel dwell time.

A series of experiments of PN codes were performed in the previous work of our laboratory, and were primarily concerned with the demonstration of the basic principle[18,19]. Recently, a series of experiments of three-dimensional imaging lidar systems using these principles has been conducted. A schematic of the system components are shown in Fig. 1. A PN code generator, a module of a field-programmable gate array (FPGA) capable of producing 1024 bits of M sequence PN codes at 1 GHz modulation rate and 10 kHz repeating rate, was connected to an optical communication module. The modulated diode laser was amplified by a three-stage fiber amplifier, and the average power of the final output laser is 260 mW. The laser's output is steered in a horizontal and vertical direction by tow motor-driven scanning reflectors. The horizontal scanning angle is 360°, while the vertical scanning angle depends on the mechanical structure of the optical system. Angle information was obtained by the encoder and transmitted to the FPGA. The return photons took the same co-axial optical path back to the receiving optical system, passed through a 10 nm band-pass filter centered at 1550 nm with a diameter of 50 mm to restrict background noise, and launched into a single mode fiber. The fiber was connected to the single-photon detector, providing electrical photon signals to the FPGA. The optical transmitting and receiving system is shown in Fig. 2. Stratix V, a high-performance FPGA, was used in the system to achieve photon counting and correlation. The program of the FPGA was designed in multithreaded architecture, which allows the simultaneous acquisition, mathematical operation,

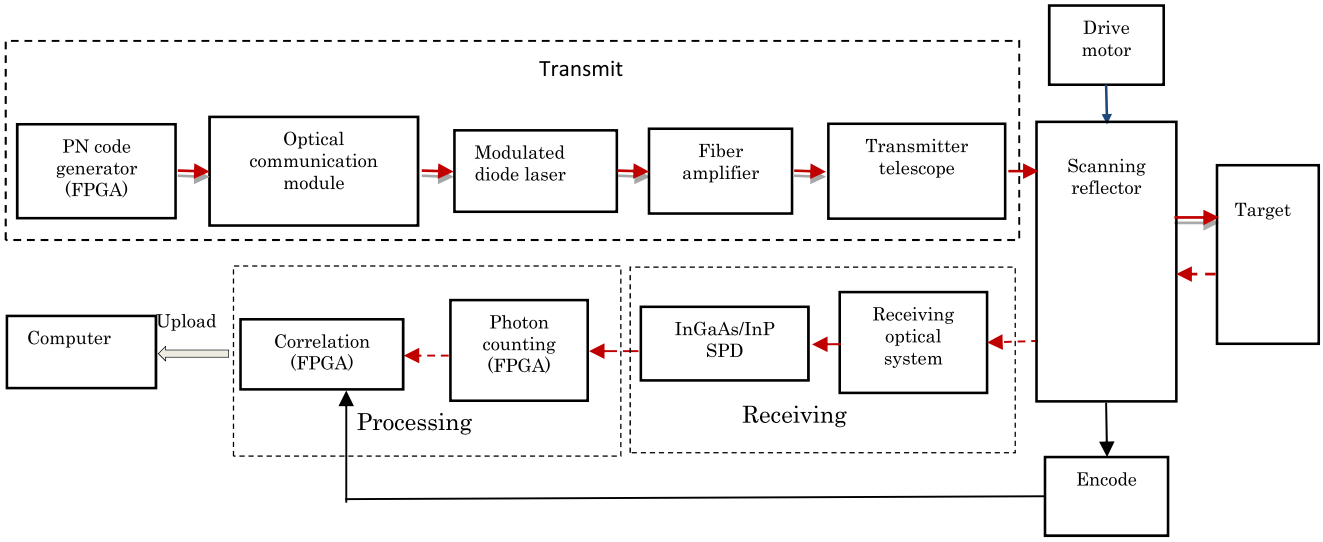

Fig. 1. Schematic of the three-dimensional imaging lidar system.

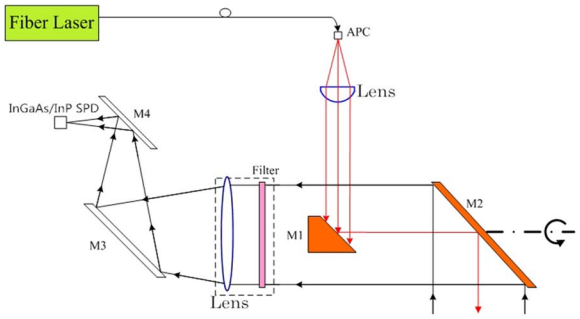

Fig. 2. Optical transmitting and receiving system.

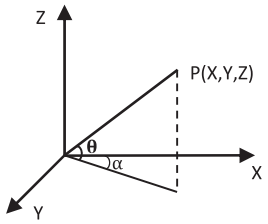

Fig. 3. Coordinate system transformation of three-dimensional imaging.

and data packing. The detail of processing is as follows: while the system acquires the sequence of electrical photon signals for the current pixel, the data are buffered in the FPGA and cross-correlated against the initial PN code to find the location of the peak which represents the range of the target. At the same time, the angle information and the range information are packaged together, and then uploaded to the computer through the Ethernet. These data can be transferred into a three-dimensional image by conversion. The coordinate system transformation is shown in Fig. 3, and the method of conversion is given by

$$\begin{cases} X = S\cos\theta\cos\alpha \\ Y = S\cos\theta\sin\alpha, \\ Z = S\sin\alpha \end{cases} \tag{1}$$

where X, Y, and Z represent the coordinates of the target, S represents the distance between the target and the lidar system, θ is the vertical scanning angle, and α is the horizontal scanning angle.

The single-photon detector used is a 1 GHz sine-wave gated InGaAs/InP avalanche photodiode in Geiger mode[20]. The detector efficiency is 10%. Usually this parameter is measured in ideal conditions (the laser pulse synchronizes with the gate; the pulse width is less than the gate opening time, and the dead-time is not taken into account). However, in the actual imaging system, these conditions are not satisfied, which will significantly reduce the number of photons that can be detected. A simulation was performed to verify the actual detector efficiency. Related parameters are shown in Table 1. The probability of a single-photon detector to producing photoelectrons obeys the Poisson distribution, which is shown as

Table 1. Simulation Parameters of Actual Detector Efficiency

Parameters	Value
Ideal detector efficiency	10%
Laser modulation frequency	1 GHz
Gate repetition frequency	1 GHz
Gate open time	300 ps
The number of signal “1” in original PN code	512
The number of photons of every signal “1” in original PN code	1
Dead-time	10 ns

$$P(N) = \frac{(N_s \times \lambda)^N}{N!} \exp(-N_s \times \lambda), \quad (2)$$

where N represents the number of photoelectrons, N_s represents the number of incident photons, and λ represents the detector efficiency. It can be assumed that the number of incident photons in each signal "1" is one, and the detector efficiency is 10%. Therefore, if only the ideal detector efficiency is taken into account, the photoelectron sequence will be as it is shown in Fig. 4(a). However, only the photons which arrived when the gate is on can be converted into photoelectrons. So, the photoelectron sequence will be as it is shown in Fig. 4(b). What is more, if the dead-time of a single-photon detector is considered, the photoelectron sequence will be as it is shown in Fig. 4(c). Figure 4(d) shows the results of 50 simulations. The simulation results show that the actual detector efficiency is about a quarter of the ideal value. An experiment was carried out to verify this result. Figure 5 shows the schematic

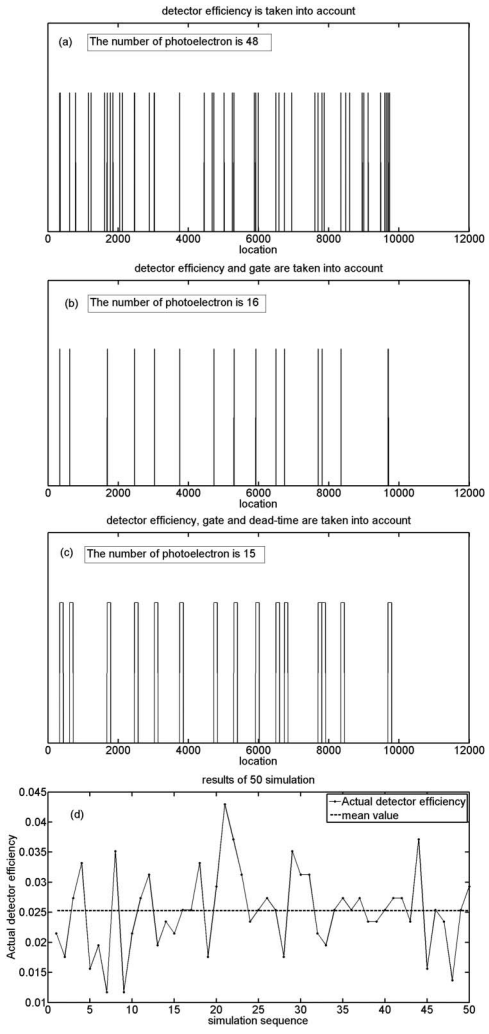

Fig. 4. Photoelectron sequence when (a) detector efficiency is taken into account, (b) detector efficiency and gate are both taken into account, and (c) detector efficiency, gate, and dead-time are taken into account. (d) The results of 50 simulations and the mean values of actual detector efficiency.

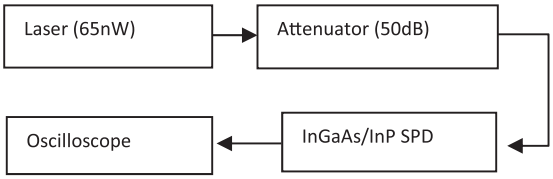

Fig. 5. Experiment system of testing the actual detector efficiency.

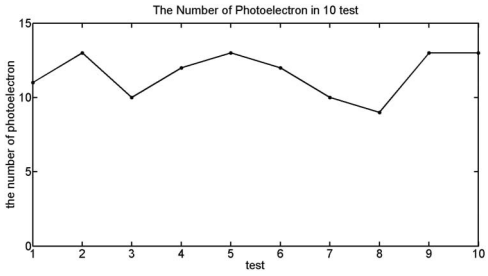

Fig. 6. Number of photoelectrons in 10 tests.

of the experiment. A 65 nW laser was attenuated by 50 dB, which means that the average number of photons in each signal "1" is one. Figure 6 demonstrates the number of photoelectrons in 10 tests. Thus, it can be calculated that the actual detector efficiency is 2.26%, which is close to the results of the simulation.

The quality of imaging depends on the precision of the ranging, so at first we implemented an outdoor ranging test in daylight. The main parameters are shown in Table 2, and the results of the 50 measurements are shown in Fig. 7. The result of the test shows that the actual ranging resolution is consistent with the theoretical limiting resolution, which means that a lidar system based on high speed PN modulation and photon counting can achieve precision ranging at a low transmitter power.

Table 2. Parameters of Outdoor Ranging Test

Parameters	Value
Target distance	859.5 m
Wavelength	1550 nm
Environmental conditions	bright
Pulse repetition frequency	10 kHz
Limiting resolution	0.15 m
Actual detector efficiency	2.26%
Transmitter average power	260 mW
Telescope aperture	50 mm
Bandwidth of filter	10 nm
PN code bit rate	1 Gb/s
PN code length	1024

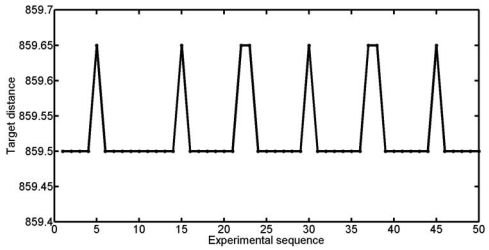

Fig. 7. Results of the 50 measurements.

Table 3. Parameters of Outdoor Three-Dimensional Imaging

Parameters	Value
Imaging range	0–1200 m
Horizontal scan angle resolution	0.07875°
Vertical scanning angle resolution	0.23625°
Pixel dwell time	100 μs
Total measurement time	30 min
Range resolution	0.15 m

Table 3 illustrates the parameters of three-dimensional imaging. Other parameters are the same as in Table 2. It should be noted that pixel dwell time is limited by a 10 kHz pulse repetition frequency in the system. If the pulse repetition frequency can be improved, the pixel dwell time can be reduced to 1.024 μs (the length of a PN code) without consideration for the range ambiguity. Compared with the pulsed photon counting system, the pixel dwell time is reduced a lot[21–23]. Figure 8 is the top view of the point-cloud representation of the three-dimensional imaging and google map of the same place. Each building is marked with a different annotation. Figure 9 is the front view of the point-cloud representation of the three-dimensional imaging and photograph of the same place. It can be seen that the three-dimensional image of the buildings have a clear outline and accurate relative positions. What is more, a lot of the details can also be seen from the figures, such as house windows, undulating terrain, and even a telegraph antenna and trees. Table 4 illustrates the signal-to-noise ratio (SNR) of landmark target. The SNR is given by

$$20 \times \log \frac{C_t}{C_b}, \tag{3}$$

where C_t represents the cross-correlation value of the target, and C_b is the cross-correlation value of the background.

In conclusion, a three-dimensional imaging lidar system based on high speed PN modulation and photon counting is proposed. The specific structure and working principle is discussed, especially the actual detector efficiency of a single-photon detector in a ranging and imaging system. The results show that the gate, dead-time, and non-synchronization between the transmission and reception will reduce the actual detector efficiency. A series of ranging and imaging experiments of 1200 m non-cooperative targets are conducted. The system obtains accurate distance data and clear three-dimensional point-cloud

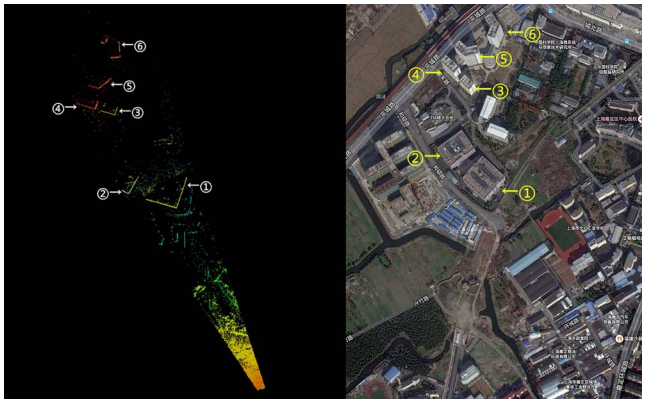

Fig. 8. Top view of the point-cloud of the three-dimensional imaging (on the left), and a google map of the same place (on the right).

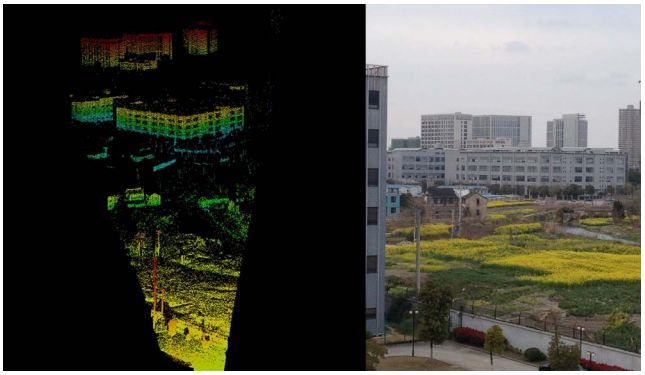

Fig. 9. Front view of point-cloud of the three-dimensional imaging (on the left), and a photograph of the same place (on the right).

Table 4. SNR of Landmark Target

Target	Distance (m)	SNR (dB)
Ground	110	17.46
Building	477	17.98
Building	595	16.65
Building	799	13.62
Building	871	13.74
Building	914	13.74
Building	963	9.14
Building	1181	5.4

images. The results show that high speed PN modulation in conjunction with photon counting technologies allows for the low-power and long distance acquisition of ranging and three-dimensional imaging. Compared with the high-power pulse lidar and the pulsed photon counting systems, the PN code lidar has the advantage of low peak power and shorter pixel dwell time, respectively. As can be seen from these advantages, the PN code lidar is a promising lidar scheme for long distance ranging and three-dimensional imaging.

We thank for Dr. Heping Zeng and Dr. Guang Wu from State Key Laboratory of Precision Spectroscopy, East China Normal University for their technical help in the InGaAs/InP APD SPD. We also appreciate the work by Dr. Jintao Liu from Ocean University of China for the technical support in FPGA PN coded circuit. This work was supported by the Innovation Fund (No. CXJJ-16M102) and the National 973 Program of China (No. 613192).

References

1. M. C. Amann, T. Bosch, M. Lescure, R. Myllyla, and M. Rioux, Opt. Eng. **40**, 1 (2001).
2. X. Liu, X. Wang, Y. Cao, S. Fan, Y. Zhou, and Y. Liu, Chin. Opt. Lett. **13**, 071102 (2015).
3. D. Lu, X. Wang, S. Fan, J. He, Y. Zhou, and Y. Liu, Chin. Opt. Lett. **13**, 081102 (2015).
4. J. Yun, C. Gao, S. Zhu, C. Sun, H. He, L. Feng, L. Dong, and L. Niu, Chin. Opt. Lett. **10**, 121402 (2012).
5. W. B. Chen, X. Hou, J. Z. Bi, D. H. Yu, Y. F. Wu, H. G. Zhang, R. Shu, and J. Y. Wang, in *Conference on Lasers and Electro-optics/Pacific Rim 2007* (2007), paper ThG1_4.
6. A. M. Pawlikowska, R. M. Pilkington, K. J. Gordon, P. A. Hiskett, G. S. Buller, and R. A. Lamb, Proc. SPIE **9250**, 925007 (2014).
7. X. Cheng, J. Wang, Z. Yang, J. Liu, L. Li, X. Shi, W. Huang, J. Wang, and W. Chen, High Power Laser Sci. Eng. **2**, e18 (2014).
8. A. W. Yu, M. A. Krainak, D. J. Harding, J. B. Abshire, X. L. Sun, S. Valett, J. Cavanaugh, and L. Ramos-Izquierdo, Proc. SPIE **7578**, 757802 (2010).
9. X. Sun, J. B. Abshire, M. A. Krainak, and W. B. Hasselbrack, Proc. SPIE **6771**, 67710O (2007).
10. M. Dobbs, W. Krabill, M. Cisewski, F. W. Harrison, C. K. Shum, D. McGregor, M. Neal, and S. Stokes, in *Conference on Lasers and Electro-Optics and Quantum Electronics and Laser Science Conference* (2009), paper CFJ5.
11. J. Abshire, X. Sun, and M. A. Krainak, in *Conference on Lasers and Electro-Optics* (2005), paper JThI4.
12. Y. Emery and C. Flesia, Appl. Opt. **37**, 2238 (1998).
13. X. L. Sun and J. B. Abshire, Proc. SPIE **7199**, 71990P (2009).
14. Y. Liang, J. Huang, M. Ren, B. Feng, X. Chen, E. Wu, G. Wu, and H. Zeng, Opt. Express **22**, 4 (2014).
15. Z. Li, Z. Bao, Y. Shi, B. Feng, E. Wu, G. Wu, and H. Zeng, IEEE Photon. Technol. Lett. **27**, 6 (2015).
16. Z. Bao, Y. Liang, Z. Wang, Z. Li, E. Wu, G. Wu, and H. Zeng, Appl. Opt. **53**, 3908 (2014).
17. Z. Bao, Z. Li, Y. Shi, E. Wu, G. Wu, and H. Zeng, IEEE Photon. Technol. Lett. **26**, 15 (2014).
18. X. Zhang, F. Yang, Y. Liu, Y. He, X. Hou, and W. B. Chen, Opt. Eng. **52**, 12 (2013).
19. F. Yang, X. Zhang, Y. He, and W. Chen, Chin. Opt. Lett. **12**, 082801 (2014).
20. M. Ren, X. R. Gu, Y. Liang, W. B. Kong, E. Wu, G. Wu, and H. P. Zeng, Opt. Express **19**, 14 (2011).
21. L. Sjöqvist, M. Henriksson, P. Jonsson, and O. Steinvall, Adv. Opt. Technol. **3**, 2 (2014).
22. A. McCarthy, N. J. Krichel, N. R. Gemmell, X. Ren, M. G. Tanner, S. N. Dorenbos, V. Zwiller, R. H. Hadfield, and G. S. Buller, Opt. Express **21**, A7 (2013).
23. N. J. Krichel, A. McCarthy, and G. S. Buller, Opt. Express **18**, 9192 (2010).